Smart Materials in Manufacturing 4 (2026) 100129

Contents lists available at ScienceDirect

Smart Materials in Manufacturing

journal homepage: www.keaipublishing.com/en/journals/smart-materials-in-manufacturing

Research Paper

Guided diffusion for fast inverse design of voxel-based mechanical metamaterials

Yanyan Yang [a,1], Lili Wang [a,1], Xiaoya Zhai [a,*], Kai Chen [b], Wenming Wu [c], Yunkai Zhao [a], Falai Chen [a], Ligang Liu [a], Xiao-Ming Fu [a,*]

[a] School of Mathematical Sciences, University of Science and Technology of China, Hefei, Anhui 230026, PR China
[b] Zhongguancun Institute of Artificial Intelligence, Beijing 100194, PR China
[c] Hefei University of Technology, Hefei, Anhui 230026, PR China

ARTICLE INFO

Dataset link: Google Drive

Keywords:
Guided diffusion model
Inverse design
Mechanical metamaterials
Multiscale design

ABSTRACT

Mechanical metamaterials are synthetic materials that can possess extraordinary physical characteristics, such as abnormal elasticity, stiffness, and stability, by carefully designing their structure. The representation of metamaterials through high-resolution voxels has the potential to reveal delicate local structures with unique mechanical properties. However, this approach results in a substantial computational burden. To this end, this paper proposes a fast inverse-design framework driven by a self-conditioned diffusion model. An initial set of microstructures is first generated using a physics-based optimization algorithm and used to train the diffusion model. The trained model is then employed to synthesize new candidate microstructures, from which high-quality samples are selected and incorporated into the training set for subsequent retraining. By iterating this generate–filter–retrain cycle, we progressively construct a large-scale dataset and obtain a high-performance generative model. Our model is capable of generating a microstructure to approach the specified homogenized tensor matrix in just 0.42 s on an NVIDIA GeForce RTX 3090 GPU. Compared with the state-of-the-art gradient-based topology optimization method, we achieve an average acceleration of 100 times. Furthermore, we demonstrate that the proposed model enables efficient exploration of extreme metamaterial designs, supports multiscale design workflows, and, through a dedicated guidance mechanism, generates families of metamaterials with continuous variations in both geometry and physical properties. This flexible and adaptive generative tool is of great value in structural engineering or other mechanical systems and can stimulate more subsequent research.

1. Introduction

Architectured metamaterials, a novel frontier in materials research, have opened up new possibilities for creating materials with unique and unconventional functionalities. They offer precise control over a range of physical properties, including mechanical strength [1–3], Poisson's ratio [4–8], and buckling behavior [9–11]. The surveys [12–14] provide a comprehensive overview of the research progress in mechanical metamaterials.

Once the properties of the base material are given, the mechanical properties of the metamaterial are determined by its geometry. Mathematically, geometry can be expressed in various forms, such as parametric functions, implicit functions, discrete meshes, and voxel representations. Voxel representation has two main advantages compared with other representations: (1) it is flexible for representing various geometries, thus possessing various mechanical properties, and (2) it is regular and simple, reducing the design difficulty of the metamaterial generation algorithm. Moreover, high-resolution metamaterials represented by a large number of voxels can have delicate local structures, thus showing exciting mechanical properties.

Voxel-based metamaterials are generally obtained using the topology optimization method to solve the inverse homogenization problem [15]. However, this method has three limitations due to the large design space, which is based on density. First, high-resolution topology optimization still requires expensive computing resources and considerable computing time, although various excellent algorithms have been proposed, such as the multi-CPU framework [16–18], GPU computation [19–22], and adaptive mesh refinement [23]. Second, since the optimization problem is highly nonlinear and nonconvex,

Peer review under the responsibility of Editorial Board of Smart Materials in Manufacturing.
* Corresponding authors.
E-mail addresses: xiaoyazhai@ustc.edu.cn (X. Zhai), fuxm@ustc.edu.cn (X.-M. Fu).
[1] These authors contributed equally to this work.

https://doi.org/10.1016/j.smmf.2026.100129
Received 31 August 2025; Received in revised form 29 November 2025; Accepted 24 February 2026
Available online 2 March 2026

the optimized metamaterials are closely related to the initialization. In practice, there is almost no rule for choosing initial metamaterials to be optimized with high stiffness (or values near the theoretical limits), and we can only perform tedious trial and error. Third, due to the high computational burden and the dependence on initial metamaterials, diverse generated metamaterials have poor geometric connectivity, and it is challenging to create metamaterial sequences with extreme mechanical properties, thereby decreasing their performance in multiscale design [24,25]. The data-driven inverse design of mechanical metamaterials is a possible way to address these limitations [26]. Recently, evolutionary strategy-based and deep learning-driven inverse design frameworks have further advanced this field [27,28]. It can inversely design mechanical metamaterials [29–32] and quickly assemble and generate multiscale systems [33,34]. Specifically, since the goal of a deep generative AI model is highly similar to that of an inverse design algorithm, which is to generate a microstructure meeting specific requirements, deep generative AI models have been widely used to create microstructures [35,36]. Moreover, recent studies have demonstrated that programmable structural design and tunable deformation mechanisms further enhance the versatility of metamaterials in functional applications [37–41]. Collectively, these works highlight current trends toward intelligent, reconfigurable, and multiscale design paradigms, reinforcing the relevance of the proposed data-driven approach to the broader field of architected metamaterials. In addition to the representation of models, datasets play a crucial role in this kind of algorithm. The existing microstructure datasets mainly include three types: (1) low-resolution datasets using pixel/voxel representation [42–44], (2) datasets with varying geometric parameters such as the width of the truss [45–47], and (3) implicit surface-based datasets that mainly contain triply periodic minimal surfaces (TPMS) [48] and spinodoid surfaces [29]. Unfortunately, the current datasets exhibit limitations. For instance, many databases are configured in either 2D pixel or 3D voxel structures with low resolutions, which significantly restricts the performance of these datasets. While structures represented by geometric parameters have fewer design variables, their coverage of performance space is also limited. The implicit representation of datasets belongs to a specific function class, which is more suitable for certain scenarios; for example, the spinodoid structure dataset is ideal for bionic bone structure optimization. Therefore, the need for advanced data-driven methods and the generation of high-resolution voxel-based datasets with high property coverage to explore mechanical metamaterials is becoming increasingly urgent.

We construct a voxel-represented mechanical metamaterial dataset at a high resolution of 128^3, with partial coverage of modulus variations. Each metamaterial is obtained using the LIVE3D framework [22], which requires only a GPU. Specifically, the bulk modulus, shear modulus, and Poisson's ratio are the optimization objectives, and the constrained volume fraction ranges from 0.2 to 0.9. Furthermore, isotropic constraints are added to optimize part of the microstructures. Thus, the optimized dataset includes both isotropic and anisotropic metamaterials.

This paper introduces a fast inverse design method to generate voxel-based mechanical metamaterials. Central to the technique is the adoption of the self-conditioned diffusion model (an advanced deep generative AI algorithm), which produces a microstructure with a resolution of 128^3 to approach the specified homogenized stiffness tensor matrix in just 0.42 s on an NVIDIA GeForce RTX 3090 GPU, which is about 100 times faster than the state-of-the-art gradient-based topology optimization algorithm [22]. This algorithm substantially enhances the efficiency of the microstructure inverse design. Since the initial dataset only partially covers modulus variations, we apply an active learning technique to train the diffusion model and augment the dataset alternately. This results in a dataset featuring more diverse shapes, broader coverage of modulus values, and a diffusion model with higher generation accuracy.

Consequently, the model is successfully used for efficient inverse design, facilitating the exploration of extreme metamaterials, sequence interpolation in metamaterials, and the generation of diverse microstructures. First, the diffusion model has been proven to be effective in generating initial microstructures for subsequent traditional topology optimization. For example, we use the diffusion model to construct an initial microstructure with a negative Poisson's ratio of -0.54 and then realize the final extreme metamaterial with a negative Poisson's ratio of -0.63 through subsequent topology optimization. Second, according to the interpolation capability of the diffusion model, we generate a series of microstructure sequences that closely approach the theoretical upper limit. Finally, since the diffusion model can generate geometrically diverse microstructures, it is more likely to have high geometric connectivity while approaching the target properties in multiscale design.

2. Preliminary

2.1. Inverse homogenization method

Topology optimization (TO) is a computational design method that optimizes material distribution within a given design space, subject to prescribed constraints, in order to achieve optimal performance. It is widely used in structural and material design, particularly in additive manufacturing [49,50], aerospace [16,49], and mechanical engineering [51]. Unlike traditional shape and size optimization, TO allows the creation of novel, complex structures that maximize efficiency and performance.

Inverse Homogenization [52] is a computational design approach used to create microstructures with tailored effective material properties. It is commonly applied in designing metamaterials, composite materials, and architected structures for applications in mechanical, thermal, and acoustic engineering. Unlike classical topology optimization, which optimizes macroscopic structures, inverse homogenization focuses on designing periodic microstructures that exhibit desired macroscopic properties.

Fundamentals of homogenization theory. Homogenization is a mathematical technique that estimates the effective properties of heterogeneous materials by averaging their microscale behavior. This approach is essential for modeling composites and metamaterials where microstructural features dictate macroscopic properties. In general, the effective (homogenized) properties of a periodic microstructure are computed using the Representative Volume Element (RVE), which satisfies the governing equations of elasticity:

$$\nabla \cdot \boldsymbol{\sigma} = 0, \tag{1}$$

where $\boldsymbol{\sigma}$ is the stress tensor. The effective stiffness tensor $\mathbf{C}^H$ is derived by solving the cell problem:

$$C^H_{ijkl} = \frac{1}{V}\int_V C_{ijkl}(\varepsilon^*_{pq} + \varepsilon^0_{pq})\, dV, \tag{2}$$

where ε^*_{pq} is the microstructural strain field due to periodicity conditions, and ε^0_{pq} is the macroscopic strain.

Inverse homogenization problem formulation. In contrast to direct homogenization, which determines effective properties from a given structure, inverse homogenization seeks to design a microstructure that meets prescribed effective properties. The optimization problem can be formulated as:

$$\min_{\rho} \quad \|\mathbf{C}^H(\rho) - \mathbf{C}^{\text{target}}\|, \tag{3}$$

$$\text{subject to} \quad g_i(\rho) \le 0, \quad i = 1, 2, \ldots, m; \tag{4}$$

$$0 \le \rho \le 1. \tag{5}$$

where density field ρ represents the material distribution in the Representative Volume Element (RVE). $\mathbf{C}^H(\rho)$ is the computed effective stiffness tensor. $\mathbf{C}^{\text{target}}$ is the desired effective stiffness tensor. $g_i(\rho)$ are constraints such as volume fraction or manufacturability.

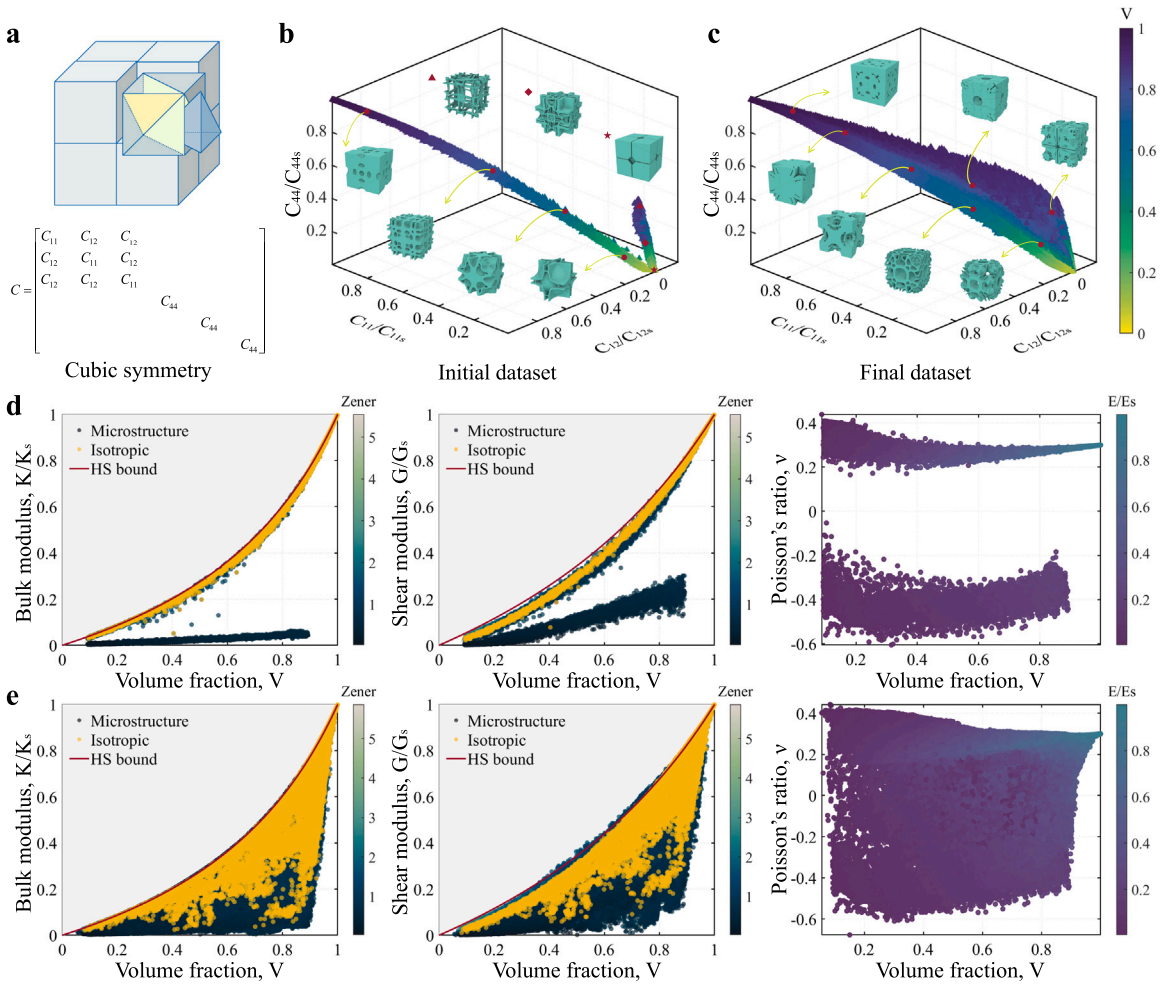

Fig. 1. Overview of the voxel-based metamaterial dataset. **a** Cubic symmetry and stiffness tensor. **b** Initial dataset. The subscript 's' represents the properties of the base material. **c** Final dataset. **d** Bulk modulus, shear modulus, and Poisson's ratio of the initial dataset. **e** Bulk modulus, shear modulus, and Poisson's ratio of the final dataset.

2.2. Multiscale topology optimization

Multiscale topology optimization (MSTO) [26,52] is a computational approach that optimizes structures at both macroscopic and microscopic scales. MSTO integrates classical topology optimization with homogenization techniques, ensuring that microstructural features enhance macroscopic performance. Multiscale modeling in topology optimization is based on the separation of scales principle, where a structure consists of a macroscopic scale and a microscopic scale. The macroscopic structure is the overall structural domain that must satisfy mechanical, thermal, or multiphysics constraints. For the microscopic structure, the periodic or non-periodic microstructure dictates the effective properties of the macroscopic material. To link the two scales, homogenization theory is employed.

MSTO always restricts the microstructures used to certain subsets of microstructures, and describes them with a few shape parameters. Sometimes, it even describes a microstructure with a single variable density. Then we can model the inverse design on both the macroscopic and microscopic scales into the following optimization problem:

$$\min_{\rho} \quad f(\mathbf{C}^H(\rho)), \tag{6}$$

$$\text{subject to} \quad g_i(\rho) \le 0, \quad i = 1, 2, \dots, m; \tag{7}$$

$$0 \le \rho \le 1. \tag{8}$$

Here ρ is a single density variable for each microstructure rather than a density field for each microstructure, f is the objective function on the macroscopic scale. $g_i(\rho)$ are constraints on macroscopic scale such as volume fraction or manufacturability. In this approach, the density field of each microstructure is simplified to a single density variable, which makes the computation feasible, but significantly restricts the shape of the microstructures.

In this paper, we employ another approach. The optimization is first carried out individually on the macroscopic scale to obtain the target homogenized stiffness tensor for all microstructures. The optimization problem is formulated as follows:

$$\min_{\mathbf{C}^H} \quad f(\mathbf{C}^H), \tag{9}$$

$$\text{subject to} \quad g_i(\mathbf{C}^H) \le 0, \quad i = 1, 2, \dots, m; \tag{10}$$

Then, Eq. (3) can be used to calculate the material distribution for each microstructure. However, solving a separate optimization problem for each microstructure is impractical. Therefore, in practice, we use our generative model to obtain microstructures that match the target homogenized stiffness tensor.

3. Methods

3.1. Data generation

Data format. Voxel-based microstructures are obtained by the inverse homogenization method in a cube domain. The cube is discretized into n voxel elements, with each element assigned a density value of

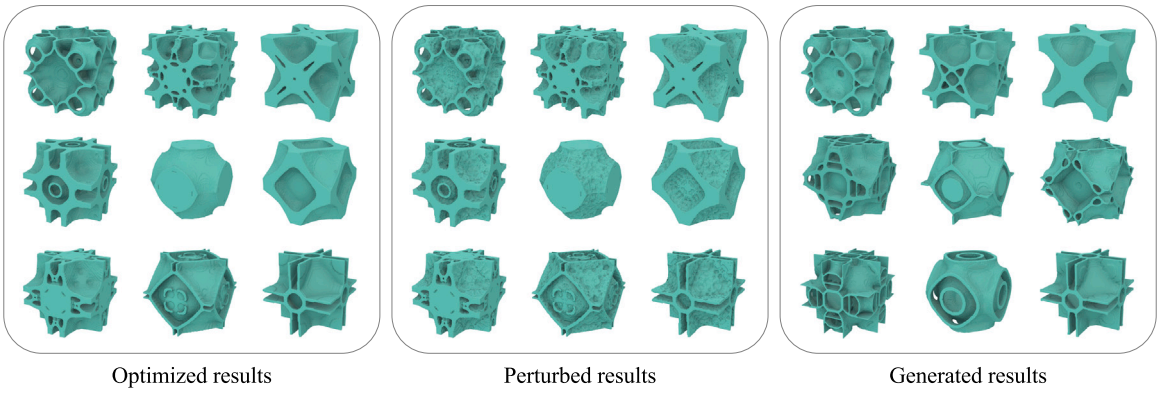

Fig. 2. Comparison between perturbed results and generated results.

0 (void) or 1 (solid). Various combinations of 0 and 1 give rise to different microstructures, resulting in 2^n combinations. The number of microstructure variations expands exponentially with the resolution parameter n. Consequently, voxel-based representations exhibit significant representational capabilities. However, it is essential to note that not all combinations yield satisfactory microstructures, and the large amount of data may impose a considerable burden on subsequent training and machine learning algorithms. When constructing the dataset, we consider the cube symmetry employing $1/8$ of unit cell lattice to simplify the representation (Fig. 1a). Subsequently, symmetric operations are applied to the $1/8$ unit cell lattice. This process ultimately leads to a cubic symmetric microstructure to facilitate calculation. To create a sufficiently large design space for a metamaterial database based on voxels, we establish microstructures at a resolution of 128^3 and subsequently store $1/8$-th of it, equivalent to 64^3 microstructures. The representation is the basis for assembling a dataset incorporating a sizable assortment of voxel-based lattices, effectively capturing a broad range of mechanical properties.

Initial dataset generation. To construct the initial metamaterial dataset, we use the LIVE3D framework [22] to optimize a collection of metamaterials (Fig. 1b). Specifically, trigonometric functions are adopted to cover various initial density fields. The basis functions of the initialization are $\{\cos 2\pi k\boldsymbol{x}, \sin 2\pi k\boldsymbol{x}\}$ $(0 < k \leq n)$, where $\boldsymbol{x} \in \mathbf{R}^3$ is the coordinate of the element's center. We formulate the optimization model with the modulus as the objective function and the volume constraint. Consequently, the constructed dataset has partial coverage of modulus variations.

Data expansion. As shown in Fig. 1, the initial dataset consists of only microstructures with either a high modulus or low Poisson's ratio. Consequently, the coverage range is limited.In the following, we describe the procedure used to construct the final dataset shown in Fig. 1c. Previous methods [44,53] use perturbations to extrapolate substantial datasets from limited datasets. We also try a three-dimensional perturbation method, yet the outcomes fall short of the ideal. Specifically, the surfaces of the structures derived through perturbation consistently exhibit characteristics reminiscent of potholes. Consequently, we ultimately chose to use active learning to expand the dataset. Fig. 2 shows a comparison between active learning and perturbation. The perturbation method is an iterative process in which we locally apply elastic deformation to specified structures at each step. The deformation field is characterized by random Gaussian noise. For the active learning method, we randomly selected 9 microstructures from the final dataset, which were generated by the previous generation of the generative model. Then, we identified the most similar microstructures in the initial dataset. These 9 generated results can be considered as inheriting some features of the optimized ones. Additionally, we display 9 microstructures obtained by perturbing these optimized structures. We observed that the perturbed structures have irregular surfaces, whereas the generated structures perfectly retain the smooth surface characteristics of the optimized structures. From this perspective, active learning can be seen as a very high-quality perturbation method.

Instead, we propose the use of active learning to augment the dataset. In essence, active learning means repeatedly taking the results generated by the previous model and putting them back into the training set for further training. With each iteration, the data become richer. Due to the high fidelity of the generative model, it maintains its quality. The improved dataset results in higher accuracy and an expanded generative scope for the model. Then, in the subsequent iteration, the more powerful generative model will produce even richer data.

The generative model may occasionally generate unreliable results. If they are left in the training set for further training, the model's reliability will significantly diminish. Since we are generating one-eighth of unit cells, there are two potential types of unreliable generation results: (1) lack of connectivity, leading to disconnected unit cells, and (2) absence of voxels at the boundary, leading to either disconnected or lacking voxels at the boundary, which violates the assumptions of homogenization theory. After removing these two types of undesirable results, further data cleaning is necessary. We remove excessively dense data points in the $C_{11} - C_{12} - C_{44} - V$ space to ensure a uniform data distribution, thus preventing bias in the model.

After undergoing three cycles of generation, cleaning, data augmentation, and retraining, we eventually obtained a comprehensive dataset that looks like the convex hull of the initial dataset. Our final dataset is obtained through three rounds of active learning. Fig. 3 shows the dataset for each round. Our initial dataset consists of 14,396 microstructures from a voxelized optimization algorithm. Since the dataset expanded by the perturbation method approximately covers the closure of the initial dataset, we aimed for active learning to achieve a similar or better effect. In the first round, we randomly generate 8000 microstructures with specific stiffness tensors within or just outside the boundary of the perturbation dataset range. Specifically, we calculated a Signed Distance Function (SDF) to represent the range of the perturbation dataset and randomly generate stiffness tensors with $f_{SDF} > -0.025$. Using these tensors as generation conditions, we obtain a second-generation dataset containing 22,396 structures. Next, we generate 20,000 microstructures in the same manner, and after removing 53 invalid structures (those with no voxels on the boundaries), we obtain a third-generation dataset containing 42,343 microstructures. For the final iteration, we generate 80,000 microstructures with $f_{SDF} > -0.025$ and 50,000 microstructures with $f_{SDF} > -0.5$. The former operation aims to fill the convex hull of the initial dataset, while the latter operation attempts to expand the dataset coverage further outward. After removing invalid structures, we obtained the final dataset containing 144,054 microstructures.

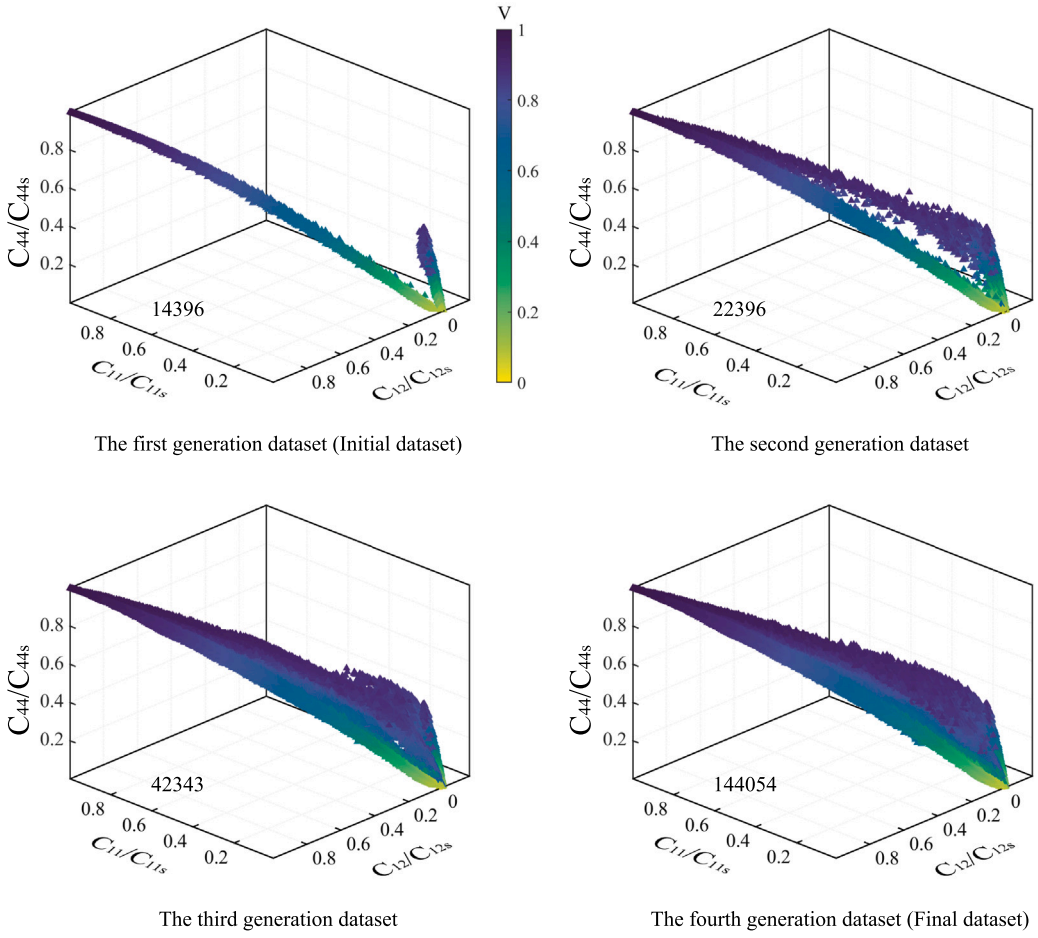

Fig. 3. Four generations of datasets with each containing 14396, 22396, 42343, and 144054 data pairs.

Data statistics. The total optimization results consist of 10,000 structures optimized for bulk modulus and 4396 structures optimized for Poisson's ratio. The volume fractions considered in the optimization range from 0.05 to 1. After iterative augmentation via active learning, our final dataset comprises 144,054 microstructures, as illustrated in Fig. 1. However, the distribution of these 144,054 data points in the $C_{11}-C_{12}-C_{44}-V$ space is uneven. To prevent uneven data distribution from causing instability during training and reducing the accuracy of the generated results, the excessive data is removed from overly dense regions to ensure a more uniform distribution, resulting in a training set containing 21,212 data points.

By examining Figs. 1d–e and 3, it can be observed that, from multiple perspectives, whether in terms of the stiffness tensor or various moduli, the dataset gradually covers and eventually slightly exceeds the convex hull of the initial dataset during the active learning process. This phenomenon can be attributed to the generative network's generalization capability, which is developed from a large number of previously seen samples. The model naturally tends to produce new data that represent combinations of geometric features from those seen samples. When reflected in material properties, such geometric combinations cause the generated materials to fall within or near the convex hull of the initial range. Furthermore, those data points that slightly exceed the convex hull enable the well-trained model to assist in exploring extreme materials, which precisely embodies one of the key purposes of a generative model.

3.2. Framework of the diffusion model

Recent advances in diffusion models [55] have significantly improved the generation stability and controllability of diffusion-based generative frameworks. Unlike traditional generative models such as GANs or VAEs, which learn a direct mapping from latent space to data space, diffusion models gradually learn to reverse a well-defined noising process, resulting in superior sample fidelity and diversity. Furthermore, the self-conditioning mechanism [56] introduces an additional feedback loop by reusing the model's previous prediction of the clean sample as an auxiliary input in the next denoising step.

As described in Denoising Diffusion Probabilistic Models (DDPM) [57], a diffusion model comprises forward and reverse processes. In the forward process, Gaussian noise is incrementally introduced to the data point x_0 until it evolves into pure Gaussian noise, denoted as x_T, which can be defined as follows:

$$x_t = \sqrt{\gamma_t} x_0 + \sqrt{1-\gamma_t}\epsilon, \tag{11}$$

where $\epsilon \sim \mathcal{N}(0, I)$ and γ_t monotonically decreases from 1 to 0. The reverse process restores Gaussian noise x_t to a data point x_0 by denoising it step by step, this process is shown in Supplementary Fig. 3. At each step, the prediction of x_{t-1} from x_t is facilitated by a neural network, typically a U-Net, which predicts x_{t-1}, ϵ, or x_0. In our work, we use a U-Net $f(x_t, \hat{x}'_0, t, \text{conditions})$ to predict x_0, where $\hat{x}'_0$ is an estimation of x_0 from the previous prediction, which is introduced by self-conditioning technique [56]. By reusing the model's previous estimations as auxiliary inputs for subsequent denoising steps, the model effectively retains and refines information across iterations, enabling it to generate results that are more consistent and better aligned with the given conditions. During training, $\hat{x}'_0$ is set to $f(x_t, 0, t, \text{conditions})$ with 50% probability; otherwise, it is set to 0. The conditions include the stiffness tensor (C_{11}, C_{12}, C_{44}) and volume fraction. We first normalize C_{11}, C_{12}, and C_{44} into $[0, 1]$ separately. Then, the condition's four components are

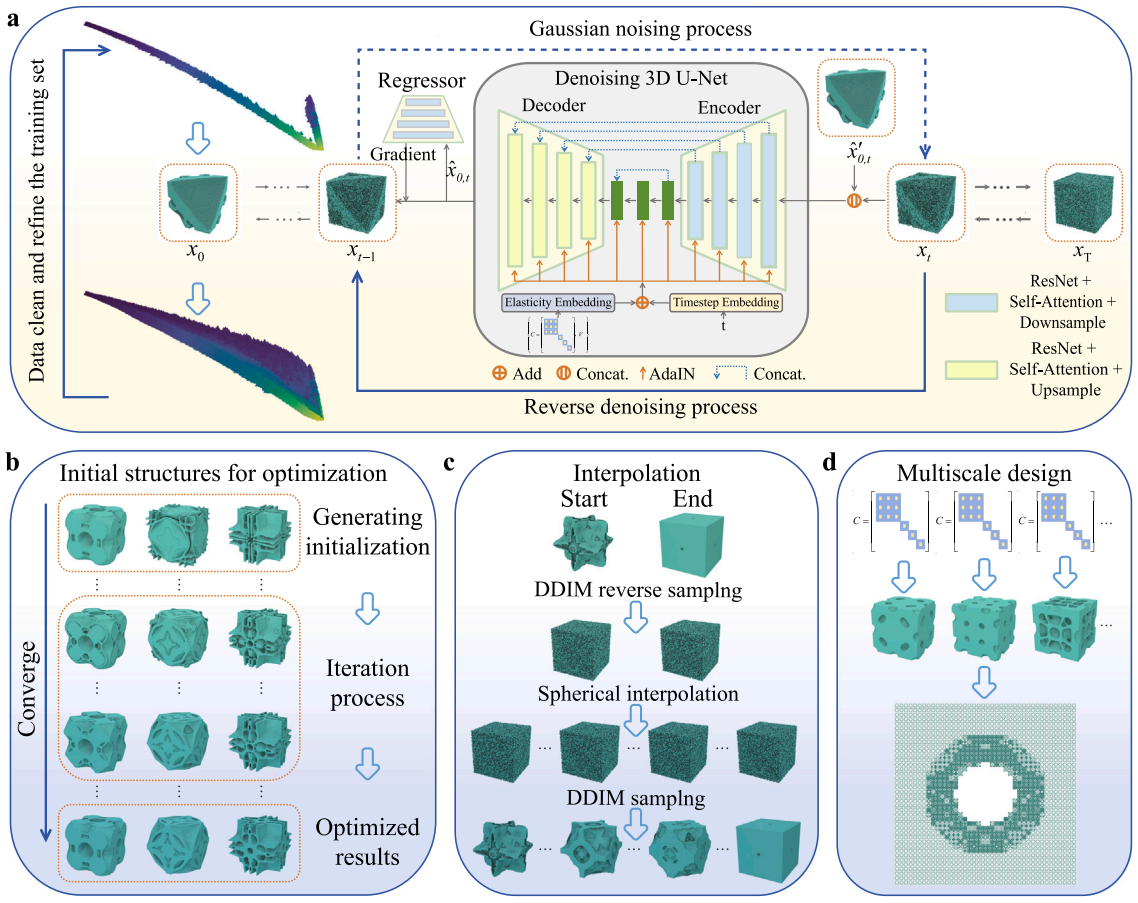

Fig. 4. Generative model framework and its three applications. a Framework of the diffusion model. **b** Using generated results as initials to do optimization approaching extreme. **c** Properties and shape interpolation of microstructure sequences based on the denoising diffusion implicit model (DDIM) [54]. **d** Multiscale design.

encoded by learnable sinusoidal embeddings and integrated into the model through classifier-free guidance [58]. By setting them to a predetermined special value (we use −1 in the experiments) separately or simultaneously, we can generate structures conditioned solely on either the stiffness tensor or the volume fraction or without conditions. The loss function is:

$$\mathcal{L}_{x_0} = E_{\epsilon\sim\mathcal{N}(0,I),t\sim U(0,I)}\|\hat{x}_0 - x_0\|_2^2, \tag{12}$$

where

$$\hat{x}_0 = f(x_t, \hat{x}_0', t, \text{conditions}). \tag{13}$$

Since the data are cubic symmetric, we force the results to be cubic symmetric at the end of the forward process, significantly improving the network performance.

Fig. 4 shows the detailed generative model framework and its applications. The backbone denoising network is a U-Net based on the standard 3D convolutional neural network. Following LAS-Diffusion [59], U-Net is composed of 5 levels: $64^3, 32^3, 16^3, 8^3$, and 4^3, with feature dimensions gradually increasing to 32, 64, 128, 256, and 256, respectively. Each level is constructed with a ResNet block, which includes two convolution layers with a kernel size of 3. In the U-Net bottleneck, two ResNet blocks are introduced. To map the voxel features at the finest level to a surface occupancy value, a convolution layer is added after the network. We also try different U-net settings, the ablation study results can be found in Supplementary Table 4.

Training details. During training, we set the stiffness tensor to −1 with a probability of 10%, the volume fraction to −1 with a probability of 10%, and both to −1 simultaneously with a probability of 10%. We use the AdamW optimizer to train the diffusion model. The learning rate is set to 2×10^{-4}, the EMA rate to 0.999, and the model is trained for 4000 epochs. The evolution of the loss function can be found in Supplementary Fig. 4.

3.3. Universal guidance for interpolation

Specifically, universal guidance suggests that the classifier in classifier guidance can be replaced with any objective function, and its gradient can be used to guide the generation. The objective function for interpolation between microstructures is:

$$\begin{aligned} E(\hat{x}_{0,i}) = &-3f(p(\hat{x}_{0,i})) \\ &+ E_{boundary}(p(\hat{x}_{0,i}), x_{0,i-1}) \\ &+ \alpha E_{boundary}(p(\hat{x}_{0,i}), x_{0,start}) \\ &+ (1-\alpha)E_{boundary}(p(\hat{x}_{0,i}), x_{0,end}). \end{aligned} \tag{14}$$

Here, $\hat{x}_{0,i}$ is the predicted clear microstructure in the reverse denoising process for the ith microstructure in the interpolation sequence. $p(x) = tanh(64x + 1)/2$ is a projection function to force x to a 0–1 tensor. f is a regressor that predicts the ratio of the bulk modulus of the microstructure to its upper limit at the volume fraction. The regression-derived R^2 is 0.99, and the corresponding fitted scatter plot is in Supplementary Fig. 2a. $E_{boundary}(x, y) = \|x[0, :, :] - y[0, :, :]\|_2$, which measures the boundary difference between two microstructures x and y. The last three terms of the objective function correspond to the boundary differences between the currently predicted microstructure in the denoising process and the previous microstructure in the interpolation sequence, the initial microstructure, and the final microstructure. $\alpha = i/N$, where N is the length of the interpolation sequence.

3.4. Multiscale design

The multiscale optimization problem extends the 2D problem [60]. The model utilizes relative displacement difference as an objective function defined as

$$\Delta = \frac{\sqrt{\sum_{i\in\Omega_s}(\boldsymbol{u}_i - \boldsymbol{u}_{0,i})^2}}{\sqrt{\sum_{i\in\Omega_s}(\boldsymbol{u}_{0,i})^2}}, \tag{15}$$

where Ω_s represents the surrounding region, $\boldsymbol{u}_{0,i}$ is the ith nodal displacements of the reference configure (the cloak region has the same structure as the surrounding region) , while $\boldsymbol{u}_i$ represents the ith nodal displacements of the cloaked configure. To ensure that the designed microstructure with a specified stiffness tensor falls within the range that our model can generate, an additional constraint is required:

$$f_{SDF}(y_e) > 0 \quad \forall e \in \Omega_c, \tag{16}$$

where y_e represents the stiffness tensor of element e, f_{SDF} is the signed distance function of the final dataset, and $f_{SDF}(y_e) > 0$ means that y_e is within the range of the final dataset. Ω_c is the cloak region. However, optimizing with such a large number of constraints is very challenging, so we approximate these constraints with a single constraint:

$$\frac{1}{N}\sum_{e=1}^{N} S(f_{SDF}(y_e)) < \frac{1}{N}, \tag{17}$$

where $S(x) = (\tanh(-\theta x) + 1)/2$ is a projection operation [60] which transfers x into $[-1,1]$, θ is a parameter to control the steepness of the projection and set to 64.

In practice, we found that this approximate constraint does not always replace the original element constraints well. To address this, we adopt a simple but effective approach: after each optimization iteration, we project y_e with $f_{SDF}(y_e) < 0$ to the region that satisfies $f_{SDF} > 0$.

After obtaining the stiffness tensor for each unit, we use these stiffness tensors as conditions to generate 10 microstructures for each tensor. Then, dual-decomposition Markov random field optimization [60, 61] is adopted to identify the configuration with the optimal connectivity among all combinations of generated microstructures.

4. Results

All results in this section are obtained using DDIM sampling with 25 steps. Results of more sampling strategies are provided in Supplementary Table 3.

4.1. Performance of the diffusion model

Fast inverse design. As the voxel resolution progressively increases, the computational costs will correspondingly increase via traditional topology optimization methods. In essence, computer memory and computing time are enormous challenges. After fully using the hardware resources, the inverse design problem is solved by the multi-CPU framework [17] and GPU computations [22]. Nonetheless, conventional approaches typically require several hours for resolution. Our guided diffusion model for attaining one microstructure with a resolution of 128^3 requires only 0.42 s under a specified stiffness tensor.

In the following two paragraphs, we analyze the generation performance conditioned on a stiffness tensor. A similar analysis for generation conditioned on the stiffness tensor and volume fraction, or solely on the volume fraction, is provided in Supplementary Fig. 1.

Accuracy and diversity. Our primary goal is to generate diverse microstructures with prescribed stiffness tensors. For accuracy assessment, we measure the relative error of the stiffness tensor $\mathbf{C}$ as the average of the relative errors associated with its three independent components, namely, C_{11}, C_{12}, and C_{44}. The error statistics are as follows:

$$Err(\mathbf{C}^{\text{cond}}, \mathbf{C}^{\text{gen}}) = \frac{1}{3}\sum_{i\in\{11,12,44\}} \frac{\left|C_i^{\text{cond}} - C_i^{\text{gen}}\right|}{C_i^{\max} - C_i^{\min}}, \tag{18}$$

where $\mathbf{C}^{\text{cond}}$ is the target stiffness tensor as the condition of the diffusion model and $\mathbf{C}^{\text{gen}}$ is the stiffness tensor of the generated structure. C_i^{max} and C_i^{min} represent the maximum and minimum values of the term C_i for elastic tensor $\mathbf{C}$ in our dataset. The specific maximum and minimum values used in the calculations are provided in Supplementary Table 1. Fig. 5a–c show the generation accuracy on the randomly sampled test set of the stiffness tensor, with an average error of 3.08%, which is further reduced to 1.30% if we choose the best structure among the four generated structures corresponding to each target tensor. Among all 4,000 generated results, we found that all structures had voxels on the boundary, and there were 106 disconnected structures. These disconnected structures had only a small volume fraction. For these patients, we included the largest connected component in the analysis.

Our diffusion model can generate many differently shaped microstructures for the same target stiffness tensor. For the statistical analysis of diversity (and later novelty), we define the shape similarity of two microstructures of S_1 and S_2:

$$Sim(S_1, S_2) = \frac{\left|S_1 \cap S_2\right|}{\sqrt{|S_1| * |S_2|}}, \tag{19}$$

where $|S|$ denotes the number of voxels in S, and $|S_1 \cap S_2|$ is the number of intersecting voxels between the two structures S_1 and S_2. In Fig. 5e, we compute the pair-to-pair similarity between the four structures generated by each target tensor, and the results further show that we yield very different microstructures for the same target tensor.

In classifier-free guidance, we can make a trade-off between accuracy and diversity by adjusting the guidance scale. In all the experiments shown in Fig. 5, we set the guidance scale to 1. More analysis of the guidance scale can be found in Supplementary Table 2. Furthermore, training an additional regressor is required only to enable generation under any other conditions.

In our interpolation task, we use a regressor to predict the ratio between the bulk modulus K and the upper limit of the bulk modulus K_b under the same volume fraction, with a coefficient of determination $R^2 = 0.99$.

Novelty and generalizability. Additionally, our goal is not only for the model to memorize the training set but also to genuinely comprehend the relationships between the shape and properties of the microstructures. To assess the novelty, we continue to utilize the previously defined shape similarity in Eq. (19) and further define the similarity between a microstructure and a dataset as the maximum similarity between that structure and all microstructures in the dataset. Fig. 5d illustrates the similarity between the generated results and the training set, providing evidence of our model's ability to generate novel microstructures. In Fig. 5f, we further illustrate three sets of results, comparing the generated outcomes with the microstructures in the dataset that exhibit the highest similarity. We found that most generated results are closer to the target property than their most similar microstructures in the dataset. Some exhibited noticeable shape changes, while others achieve greater proximity to the target property through subtle alterations in shape. This suggests that our model has indeed learned the relationship between the shapes of microstructures and their properties. It not only provides powerful generative capabilities but also holds the potential to assist researchers in investigating the mechanisms behind various physical properties in the future.

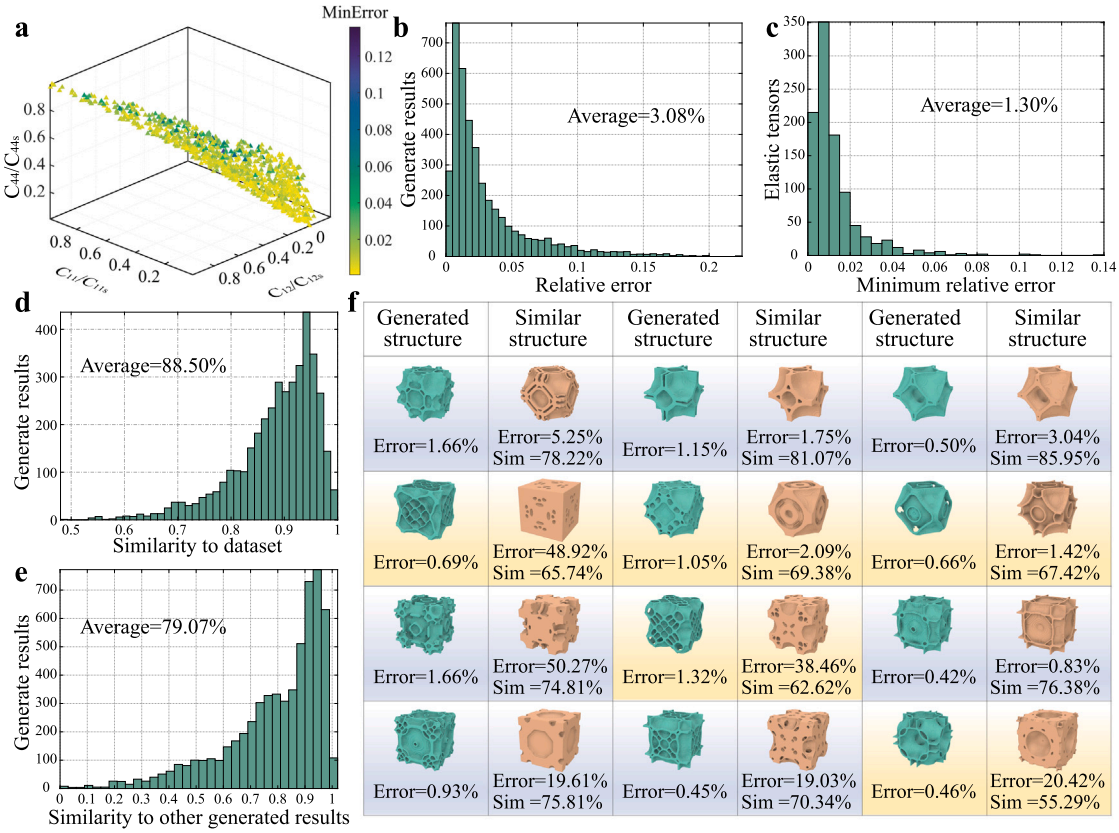

Fig. 5. Performance of the diffusion model. a–c Generalization and accuracy. We randomly take 1000 stiffness tensors from the dataset and generate 4 structures per tensor. **a** Minimum relative error of the 4 generated results for each given tensor. **b** Relative errors of all generated results. **c** Minimal relative errors of the 1000 given stiffness tensors. **d–f** Diversity and novelty. Novelty is quantified via similarity to the nearest dataset structure, while diversity is assessed through dissimilarity among four structures under the same property condition. **f** We present three sets of structures (four generated under same condition alongside their nearest dataset counterparts) to highlight diversity and novelty. Yellow/blue boxes highlight cases where shape changes significantly/minimally but improve accuracy.

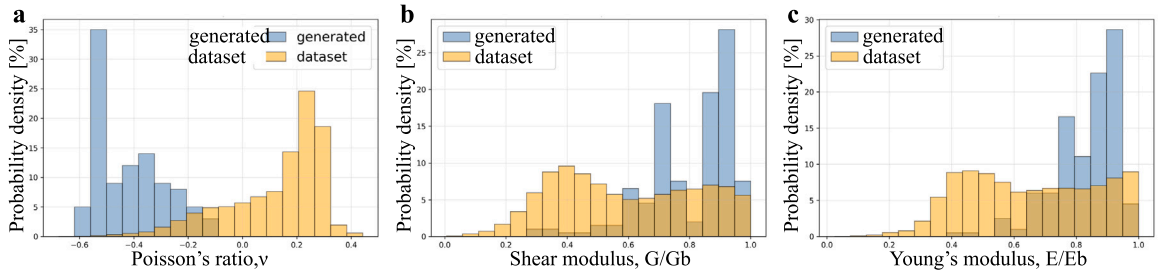

Fig. 6. Distributions of properties for final dataset vs. generated results with extreme property inputs. a Poisson's ratio distributions for the final dataset and generated samples with extremely low (negative) Poisson's ratio inputs. **b** Shear modulus distributions, normalized by the theoretical upper bound at the same volume fraction, for the dataset and generated samples with extremely high shear modulus inputs. **c** Young's modulus distributions, normalized by the theoretical upper bound at the same volume fraction, for the dataset and generated samples with extremely high Young's modulus inputs.

4.2. Exploration of metamaterials with extreme mechanical properties

We further demonstrate that the trained generative model facilitates the inverse design of metamaterials with extreme mechanical properties, including extremely low negative Poisson's ratios, as well as exceptionally high shear and Young's modulus. Fig. 6 compares the property distributions between the generated results and the dataset in three cases. The comparison shows that it is easy to generate metamaterials with extreme mechanical properties. In each of the three instances, we initially select ten microstructures from the dataset with properties close to the extreme and use their properties as generation conditions. We generate ten microstructures for each condition.

Next, we demonstrate how to combine the generative model with optimization methods to obtain materials with extreme properties that also satisfy additional requirements, such as specific volume fractions and isotropy.

Topology optimization using high-resolution frameworks has proven beneficial for exploring a broad range of metamaterials. However, it is a gradient-based optimization method whose results are closely related to the initial inputs. In other words, distinct initial values impact both the topologies and the performance of the final results. The uncertainty associated with the initial structure requires repeating the optimization process multiple times. The proposed diffusion model can provide better initial candidates for topology optimization algorithms.

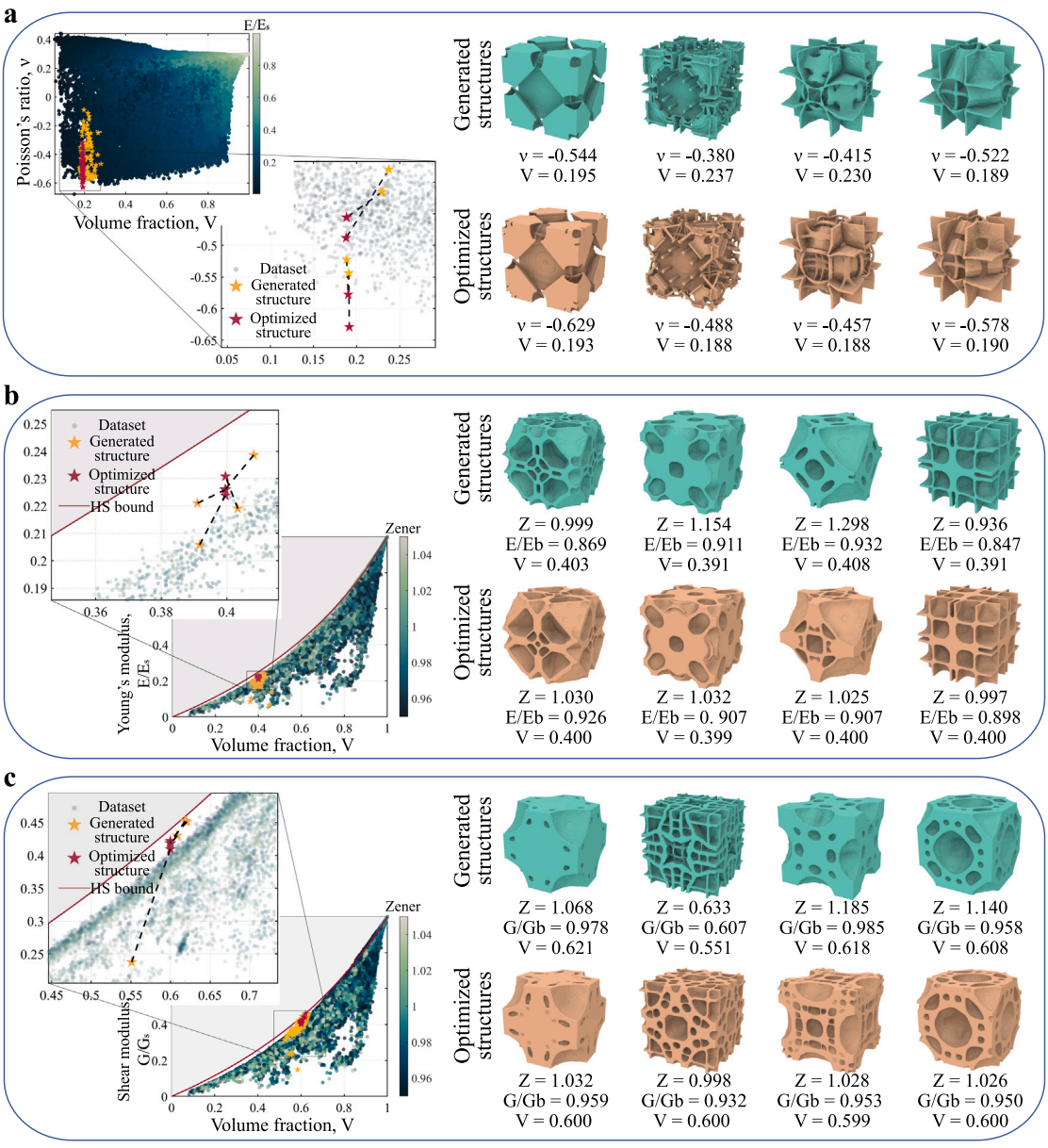

Fig. 7. Optimization with the generated structures as the initializations. For three optimization examples (**a** minimizing Poisson's ratio, **b** maximizing Young's modulus under isotropy, and **c** maximizing shear modulus under isotropy), we employ our model to generate initializations to help the optimization algorithm obtain extremer and more diverse microstructures. In each example, we select 10 microstructures close to the target in the dataset and use their properties as the generation condition to generate 100 microstructures as the initial for optimization, of which 4 structures are shown on the right side, and their properties are shown in the zooming graph.

Fig. 7 illustrates three cases of the optimal design of voxel-based microstructures for extreme properties. The structures generated in Fig. 6 are used as the initial designs for the optimization algorithm. The complete results are shown in Supplementary Fig. 5–10. In the first example, we optimize for the negative Poisson's ratio at a volume fraction of 0.2. The volume fraction and Poisson's ratio of the conditions of the diffusion model, the 100 generated results, and their corresponding optimization results are shown in Fig. 7(a,left). Four sets of these microstructures are shown in Fig. 7(a,right). We successfully optimize for a negative Poisson's ratio of −0.629, which is significantly lower than the dataset's minimum value of −0.560. Our dataset includes data from optimizing for a negative Poisson's ratio with random initializations. This comparison indicates that the initializations generated by our model outperform random initializations. In the second example (Fig. 7b), the Young's modulus is optimized under the constraints of isotropy and a volume fraction of 0.4. In the third example (Fig. 7c), the shear modulus is optimized under the constraints of isotropy and a volume fraction of 0.6. In these two examples, we first filter out microstructures in the dataset that are close to isotropic (with a Zener ratio greater than 0.95 and less than 1.05). Subsequently, we choose microstructures near the corresponding volume fraction and close to the Hashin–Shtrikman (HS) bound [62] using its stiffness tensor as the generation condition. We achieve structurally rich, isotropic microstructures with performances close to the HS bound.

In fact, our generative model provides diverse and excellent initial structures for optimization problems with various scenarios, not limited to the three cases mentioned above. This generation–optimization approach can become a universal design process that is not limited by optimization goals and constraints. We obtain richer extreme structures by selecting more generation conditions for generating more microstructures as initial structures for optimization.

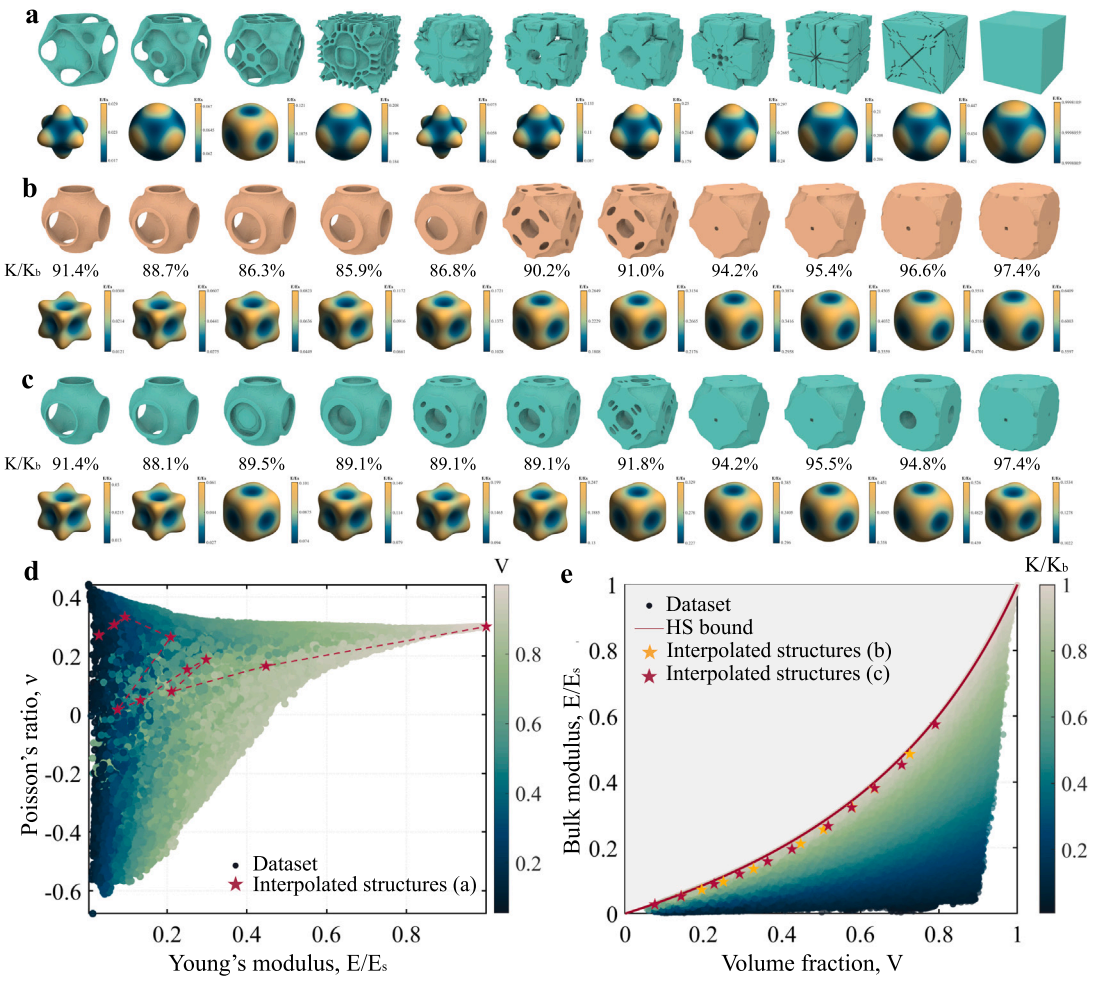

Fig. 8. Microstructure interpolation and microstructure family of extreme property. a Interpolation sequence with structures having extremely low and extremely high Young's modulus as the start and end points. **b,c** Interpolation sequence with high bulk modulus. In **b**, only noise interpolation is performed, while in **c**, universal guidance is added. **d** Interpolation trajectory in property space for **a**. **e** Interpolation trajectory in property space for **b,c**.

4.3. Microstructure interpolation

Metamaterials typically take shape through the periodic or hierarchical arrangement of individual cells. These materials must exhibit geometric connectivity [24] and maintain a continuous set of physical properties [25]. Direct generation of sequential microstructures using topology optimization methods requires extra connectivity constraints. Interpolation [55] is a common application in generative models and is particularly well-suited for generating sequential microstructures.

During sampling, we start with Gaussian noise and progressively denoise to obtain a clear structure. By reversing this process, we can deduce the corresponding noise from a clear structure. From this perspective, noise can be considered a latent space for microstructures. We perform spherical interpolation on the noise to obtain a series of continuously varying microstructures. Specifically, given the start and end structure for interpolation, we first determine their corresponding Gaussian noises, denoted as x_1 and x_2. Subsequently, we generate a series of Gaussian noises $cos(\theta)x_0 + sin(\theta)x_1$ where θ sweeps from 0 to $\pi/2$. By using this series of noises for unconditional generation, we obtain a set of microstructures that smoothly change in both geometry and physical properties.

Fig. 8a shows an interpolation application case with start and end having extreme Young's moduli, and the corresponding elastic surfaces are shown below. For such an extreme start and end, a smoothly transitioned sequence can be obtained, demonstrating the robustness of the interpolation method. Although we have not introduced physical information into the unconditional generative model, the noise of smooth transition leads to geometric shapes of smooth transition, resulting in their modulus also being smoothly transitional. However, such an interpolation solely for noise is not controllable for interpolation trajectories in the property space. This is consistent with past results [47]. As a result, there has always been a gap between microstructure interpolation and multiscale design.

After that, we modify the interpolation algorithm and obtained a family of microstructures with bulk moduli close to the HS bound and volume fractions ranging from 0.07 to 0.8, as shown in Figs. 8c and 8e. We first obtain a series of microstructures with relatively high bulk moduli by selecting the start and end microstructures with bulk modulus values close to the HS bound, as shown in Fig. 8b. However, the bulk modulus of several microstructures falls below 86% of the HS bound. Then, following the so-called universal guidance [63], we add two controls for high bulk modulus and boundary similarity during the sequence generation and obtained the sequence shown in Fig. 8c. Its bulk modulus and transition smoothness are superior to those in Fig. 8b.

4.4. Multiscale design

We employ the proposed generative model for designing a 3D mechanical cloak. As illustrated in Fig. 9, our design problem is set in a 40 × 40 × 40 cubic region. A cylinder with a radius of 20/3 is carved out (void). The annular region surrounding the cylinder, with an outer radius of 40/3, is to be filled with cloak material. The surrounding

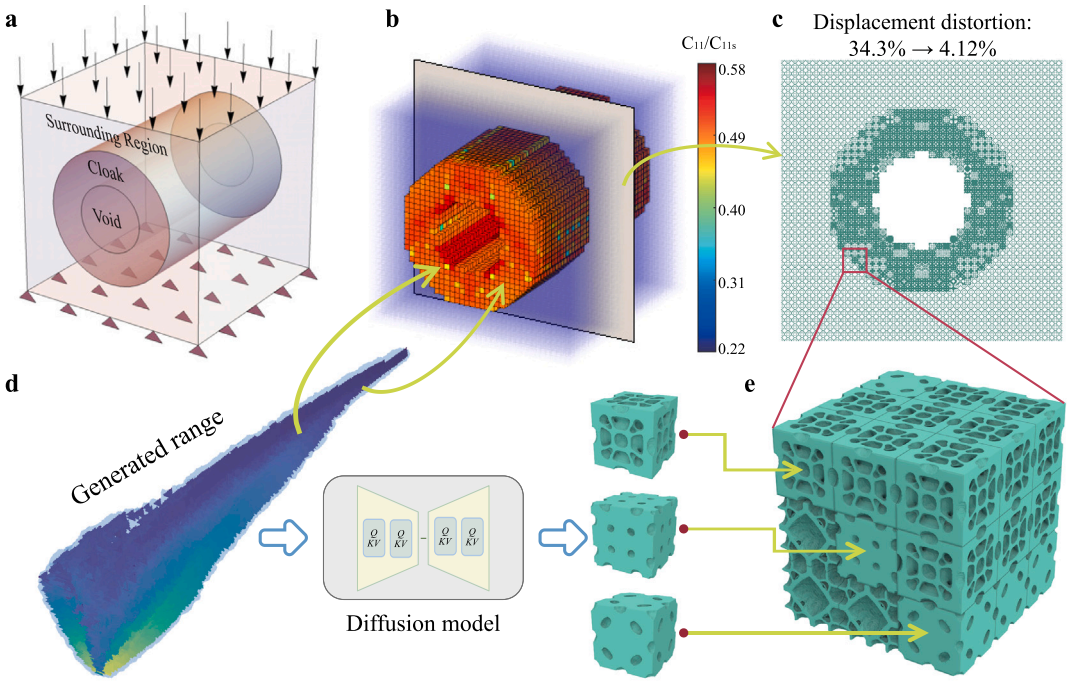

Fig. 9. Mechanical cloak via multiscale design. **a** Problem definition. **b** C_{11} distribution of optimized result. **c** A cross-section of the optimized result. **d** The range of stiffness tensors that can be generated by the generative model. **e** A 3*3 part of the optimized result.

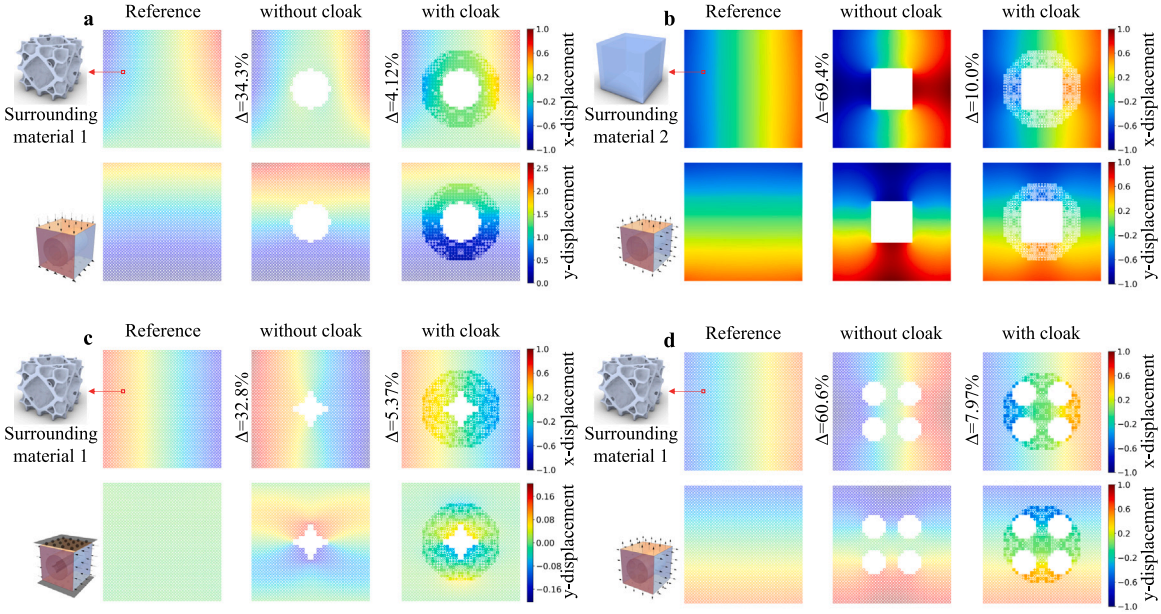

Fig. 10. Mechanical cloak design results under different boundary conditions, void shapes, and surrounding materials. Each subfigure shows the displacement field on the mid-section, with the boundary condition and void shape indicated in the lower-left corner. **a** The results of the cloak structure for a circular cylinder void under a fixed-bottom compression boundary condition with surrounding material 1. **b** The results of the cloak structure for a square cylinder void under a dilating boundary condition with surrounding material 2. **c** The results of the cloak structure for a star-shaped cylinder void under pressure-sliding boundary condition with surrounding material 1. **d** The results of the cloak structure for a four-circular cylinder void under dilating boundary condition with surrounding material 1.

region is filled with a given structure. We optimize the material properties of the cloak region and identify corresponding structures from the dataset to fill it, rendering the void mechanically invisible. In Fig. 9, our designed invisibility cloak can reduce displacement distortion from 34.3% to 4.12%. We present simulation results and additional examples under varying boundary conditions, void geometries, and surrounding materials in Fig. 10. Surrounding material 1 corresponds to an isotropic structure selected from the dataset, whereas surrounding material 2 represents a cubic thin-plate structure with a thickness of eight voxels on each face.

5. Conclusion

In this work, we present a fast inverse-design framework for mechanical metamaterials powered by an advanced deep generative model. By integrating active learning, we construct a high-quality

dataset with extensive coverage of the design space and develop a generative network that achieves both high efficiency and accuracy. The main contributions and underlying mechanisms of the proposed framework are summarized as follows:

- **High-quality dataset construction.** A high-resolution, voxel-based dataset is established by first generating an initial set of microstructures via topology optimization, followed by iterative dataset augmentation using active learning. This strategy ensures broad and representative coverage of the mechanical property space.
- **Efficient self-conditioned diffusion model.** At the core of the framework is a self-conditioned diffusion model capable of rapidly synthesizing voxel-based microstructures at a resolution of 128^3. The model accurately reproduces prescribed homogenized elasticity tensors, achieving inference times as short as 0.42 s, thereby substantially accelerating the inverse design process.
- **Multifaceted design capabilities.** The proposed method is demonstrated in three representative scenarios: (i) efficient exploration of extreme-property metamaterials, (ii) continuous interpolation within the design space for tailored mechanical responses, and (iii) generation of diverse microstructural patterns to support multiscale structural design.

Limitations and future work. The present framework focuses on generating individual microstructures with prescribed effective properties and does not explicitly account for connectivity or compatibility between neighboring unit cells. As a result, in applications such as metamaterial cloak design, an additional search procedure is required to identify suitable adjacent cells, which incurs non-negligible computational overhead. Incorporating inter-cell connectivity constraints directly into the generative design process represents a promising direction for future research.

CRediT authorship contribution statement

Yanyan Yang: Writing – review & editing, Writing – original draft, Visualization, Validation, Resources, Project administration, Methodology, Investigation, Formal analysis, Data curation, Conceptualization. **Lili Wang:** Writing – review & editing, Writing – original draft, Visualization, Validation. **Xiaoya Zhai:** Writing – review & editing, Writing – original draft, Visualization, Validation, Supervision, Resources, Methodology, Conceptualization. **Kai Chen:** Writing – review & editing, Writing – original draft, Supervision, Resources, Project administration. **Wenming Wu:** Writing – original draft, Supervision, Resources. **Yunkai Zhao:** Writing – original draft, Data curation. **Falai Chen:** Writing – review & editing, Writing – original draft, Resources. **Ligang Liu:** Writing – review & editing, Writing – original draft, Resources. **Xiao-Ming Fu:** Writing – review & editing, Writing – original draft, Project administration, Methodology, Formal analysis, Conceptualization.

Code availability

The code used to train the generative modeling framework and obtain the inverse design of voxel-based microstructures has been uploaded to GitHub.

Declaration of competing interest

The authors declare that they have no known competing financial interests or personal relationships that could have appeared to influence the work reported in this paper.

Acknowledgments

This work is supported by the National Key R&D Program of China (No. 2024YFA1016300), the National Natural Science Foundation of China (No. 62402467, No. 62025207, No. 61972368, No. 92570201), the Key Project of the National Natural Science Foundation of China (No. 12494555). Xiaoya Zhai is USTC Tang Scholar.

Appendix A. Supplementary data

Supplementary material related to this article can be found online at https://doi.org/10.1016/j.smmf.2026.100129.

Data availability

The training data, which include voxel-based microstructures and their effective homogenized properties, as well as the generated data optimized to approach the extreme and the interpolated microstructure sequences generated in this study, have been deposited in Google Drive.

References

[1] Y. Jiang, Q. Wang, Highly-stretchable 3D-architected mechanical metamaterials, Sci. Rep. 6 (1) (2016) 34147, Nature Publishing Group UK London.
[2] L.R. Meza, A.J. Zelhofer, N. Clarke, A.J. Mateos, D.M. Kochmann, J.R. Greer, Resilient 3D hierarchical architected metamaterials, Proc. Natl. Acad. Sci. USA 112 (37) (2015) 11502–11507.
[3] J.U. Surjadi, L. Gao, H. Du, X. Li, X. Xiong, N.X. Fang, Y. Lu, Mechanical metamaterials and their engineering applications, Adv. Eng. Mater. 21 (3) (2019) 1800864, Wiley Online Library.
[4] Y. Chen, T. Li, F. Scarpa, L. Wang, Lattice metamaterials with mechanically tunable Poisson's ratio for vibration control, Phys. Rev. Appl. APS 7 (2) (2017) 024012.
[5] A. Farzaneh, N. Pawar, C.M. Portela, J.B. Hopkins, Sequential metamaterials with alternating Poisson's ratios, Nat. Commun. 13 (1) (2022) 1041, Nature Publishing Group UK London.
[6] K.A. Khan, M.H. Alshaer, M.A. Khan, A novel twofold symmetry architected metamaterials with high compressibility and negative Poisson's ratio, Adv. Eng. Mater. 23 (5) (2021) 2001041.
[7] T. Li, X. Hu, Y. Chen, L. Wang, Harnessing out-of-plane deformation to design 3D architected lattice metamaterials with tunable Poisson's ratio, Sci. Rep. 7 (1) (2017) 8949, Nature Publishing Group UK London.
[8] J. Zhang, M. Xiao, L. Gao, A. Alù, F. Wang, Self-bridging metamaterials surpassing the theoretical limit of Poisson's ratios, Nat. Commun. 14 (1) (2023) 4041, Nature Publishing Group UK London.
[9] A. Ghaedizadeh, J.H. Shen, X. Ren, Y.M. Xie, Geometric bounds for buckling-induced auxetic metamaterials undergoing large deformation, Appl. Mech. Mater. 846 (2016) 547–552.
[10] S. Yves, R. Fleury, T. Berthelot, M. Fink, F. Lemoult, G. Lerosey, Crystalline metamaterials for topological properties at subwavelength scales, Nat. Commun. 8 (1) (2017) 16023, Nature Publishing Group UK London.
[11] H. Yang, L. Ma, Multi-stable mechanical metamaterials by elastic buckling instability, J. Mater. Sci. 54 (4) (2019) 3509–3526, Springer.
[12] K. Bertoldi, V. Vitelli, J. Christensen, M. van Hecke, Flexible mechanical metamaterials, Nat. Rev. 2 (11) (2017) 1–11, Nature Publishing Group.
[13] P. Jiao, J. Mueller, J.R. Raney, X. Zheng, A.H. Alavi, Mechanical metamaterials and beyond, Nat. Commun. 14 (1) (2023) 6004, Nature Publishing Group UK London.
[14] X. Yu, J. Zhou, H. Liang, Z. Jiang, L. Wu, Mechanical metamaterials associated with stiffness, rigidity and compressibility: A brief review, Prog. Mater. Sci. 94 (2018) 114–173, Elsevier.
[15] B. Hassani, E. Hinton., A review of homogenization and topology optimization I—homogenization theory for media with periodic structure, Comput. Struct. 69 (6) (1998) 707–717.
[16] N. Aage, E. Andreassen, B.S. Lazarov, O. Sigmund, Giga-voxel computational morphogenesis for structural design, Nat. 550 (7674) (2017) 84–86, Nature Publishing Group UK London.
[17] N. Aage, E. Andreassen, B.S. Lazarov, Topology optimization using PETSc: An easy-to-use, fully parallel, open source topology optimization framework, Struct. Multidiscip. Optim. 51 (2015) 565–572.
[18] T. Borrvall, J. Petersson., Large-scale topology optimization in 3D using parallel computing, Comput. Methods Appl. Mech. Engrg. 190 (46–47) (2001) 6201–6229.

[19] V.J. Challis, A.P. Roberts, J.F. Grotowski, High resolution topology optimization using graphics processing units (GPUs), Struct. Multidiscip. Optim. 49 (2) (2014) 315–325.
[20] J. Wu, C. Dick, R. Westermann, A system for high-resolution topology optimization, IEEE Trans. Vis. Comput. Graphics 22 (3) (2015) 1195–1208, IEEE.
[21] Z. Xia, Y. Wang, Q. Wang, C. Mei, GPU parallel strategy for parameterized LSM-based topology optimization using isogeometric analysis, Struct. Multidiscip. Optim. 56 (2017) 413–434.
[22] D. Zhang, X. Zhai, L. Liu, X.M. Fu, An optimized, easy-to-use, open-source GPU solver for large-scale inverse homogenization problems, Struct. Multidiscip. Optim. 66 (9) (2023) 207.
[23] R. Stainko, An adaptive multilevel approach to the minimal compliance problem in topology optimization, Commun. Numer. Methods Eng. 22 (2) (2006) 109–118, Wiley Online Library.
[24] Z. Du, X.Y. Zhou, R. Picelli, H.A. Kim, Connecting microstructures for multiscale topology optimization with connectivity index constraints, J. Mech. Des. 140 (11) (2018) 111417, American Society of Mechanical Engineers.
[25] E. Garner, H.M. A. Kolken, C.C. L. Wang, A.A. Zadpoor, J. Wu, Compatibility in microstructural optimization for additive manufacturing, Addit. Manuf. 26 (2019) 65–75.
[26] D. Lee, W. Chen, L. Wang, Y.C. Chan, W. Chen, Data-driven design for metamaterials and multiscale systems: A review, Adv. Mater. 36 (8) (2024) 2305254, Wiley Online Library.
[27] F. Dos Reis, N. Karathanasopoulos, Deep learning, deconvolutional neural network inverse design of strut-based lattice metamaterials, Comput. Mater. Sci. 244 (2024) 113258.
[28] Y. Xiang, J. Hou, X. Chen, K. Tang, X. Wang, Decoupled design of hybrid mechanical metamaterials via ensembled deep learning, Int. J. Mech. Sci. (2025) 110514.
[29] S. Kumar, S. Tan, L. Zheng, D.M. Kochmann, Inverse-designed spinodoid metamaterials, npj Comput. Materials 6 (1) (2020) 73, Nature Publishing Group UK London.
[30] X. Zheng, X. Zhang, T.T. Chen, I. Watanabe, Deep learning in mechanical metamaterials: From prediction and generation to inverse design, Adv. Mater. 35 (45) (2023) 2302530, Wiley Online Library.
[31] L. Zheng, K. Karapiperis, S. Kumar, D.M. Kochmann, Controllable inverse design of auxetic metamaterials using deep learning, Nat. Commun. 14 (1) (2023) 7563, Nature Publishing Group UK London.
[32] Q. Zeng, Z. Zhao, H. Lei, P. Wang, A deep learning approach for inverse design of gradient mechanical metamaterials, Int. J. Mech. Sci. 240 (2023) 107920, Elsevier.
[33] D. Patel, D. Bielecki, R. Rai, G. Dargush, Improving connectivity and accelerating multiscale topology optimization using deep neural network techniques, Struct. Multidiscip. Optim. 65 (4) (2022) 126.
[34] M. Seo, S. Min, DL-MSTO+: A deep learning-based multi-scale topology optimization framework via positive definiteness ensured material representation network, Comput. Methods Appl. Mech. Engrg. 415 (2023) 116276.
[35] P. Jiao, A.H. Alavi, Artificial intelligence-enabled smart mechanical metamaterials: advent and future trends, Int. Mater. Rev. 66 (6) (2021) 365–393, SAGE Publications Sage UK: London, England.
[36] J.H. Song, J.H. Lee, N. Kim, K. Min, Artificial intelligence in the design of innovative metamaterials: A comprehensive review, Int. J. Precis. Eng. Manuf. 25 (1) (2024) 225–244, Springer.
[37] J. Gu, W. Zhao, C. Zeng, L. Liu, J. Leng, Y. Liu, Construction of mechanical metamaterials and their extraordinary functions, Compos. Struct. (2025) 118872.
[38] S. Liu, Z. Niu, W. Zhao, C. Zeng, Y. Liu, J. Leng, 4D printed kirigami metamaterial with reconfigurability for dual-mode displacement-pressure sensing, Chem. Eng. J. (2025) 165392.
[39] Y. Xiang, J. Hou, X. Chen, K. Tang, X. Wang, Advanced manufacturing techniques and applications of micro-/nanoscale helices, Int. J. Extrem. Manuf. 7 (5) (2025) 052004.
[40] W. Zhao, N. Li, X. Liu, L. Liu, C. Yue, C. Zeng, Y. Liu, J. Leng, 4D printed shape memory metamaterials with sensing capability derived from the origami concept, Nano Energy 115 (2023) 108697.
[41] W. Zhao, S. Zhang, L. Geng, Y. Peng, J. Li, Y. Guo, W. Zhao, Parametric design and mechanical properties of 3D printed mechanical metamaterials based on triply periodic minimal surfaces, Thin-Walled Struct. (2025) 113572.
[42] Y.C. Chan, F. Ahmed, L. Wang, W. Chen, METASET: Exploring shape and property spaces for data-driven metamaterials design, J. Mech. Des. 143 (3) (2021) 031707, American Society of Mechanical Engineers.
[43] D. Lee, Y.C. Chan, W. Chen, L. Wang, A. van Beek, W. Chen, t-METASET: Task-aware acquisition of metamaterial datasets through diversity-based active learning, J. Mech. Des. Am. Soc. Mech. Eng. 145 (3) (2022) 031704.
[44] L. Wang, Y.C. Chan, Z. Liu, P. Zhu, W. Chen, Data-driven metamaterial design with Laplace–beltrami spectrum as shape-DNA, Struct. Multidiscip. Optim. 61 (6) (2020) 2613–2628.
[45] J.H. Bastek, S. Kumar, B. Telgen, R.N. Glaesener, D.M. Kochmann, Inverting the structure–property map of truss metamaterials by deep learning, Proc. Natl. Acad. Sci. USA 119 (1) (2022) e2111505119.
[46] N. Korshunova, I. Papaioannou, S. Kollmannsberger, D. Straub, E. Rank, Uncertainty quantification of microstructure variability and mechanical behavior of additively manufactured lattice structures, Comput. Methods Appl. Mech. Engrg. 385 (2021) 114049.
[47] L. Zheng, K. Karapiperis, S. Kumar, D.M. Kochmann, Unifying the design space and optimizing linear and nonlinear truss metamaterials by generative modeling, Nat. Commun. 14 (1) (2023) 7563, Nature Publishing Group UK London.
[48] J. Wang, W.W. Chen, D. Da, M. Fuge, R. Rai, IH-GAN: A conditional generative model for implicit surface-based inverse design of cellular structures, Comput. Methods Appl. Mech. Engrg. 396 (2022) 115060.
[49] S.S. Hanush, M. Manjaiah, Topology optimization of aerospace part to enhance the performance by additive manufacturing process, Mater. Today: Proc. 62 (2022) 7373–7378.
[50] J. Liu, A.T. Gaynor, S. Chen, Z. Kang, K. Suresh, A. Takezawa, L. Li, J. Kato, J. Tang, C.C.L. Wang, L. Cheng, X. Liang, A.C. To, Current and future trends in topology optimization for additive manufacturing, Struct. Multidiscip. Optim. 57 (6) (2018) 2457–2483.
[51] J.W. Chang, Y.S. Lee, Topology optimization of compressor bracket, J. Mech. Sci. Technol. 22 (2008) 1668–1676.
[52] J. Wu, O. Sigmund, J.P. Groen, Topology optimization of multi-scale structures: a review, Struct. Multidiscip. Optim. 63 (2021) 1455–1480.
[53] B. Zhu, M. Skouras, D. Chen, W. Matusik, Two-scale topology optimization with microstructures, ACM Trans. Graph. (ToG) 36 (4) (2017) 1, ACM NewYork, NY, USA.
[54] J. Song, C. Meng, S. Ermon, Denoising diffusion implicit models, in: International Conference on Learning Representations, 2020.
[55] P. Dhariwal, A. Nichol, Diffusion models beat gans on image synthesis, Adv. Neural Inf. Processing Syst. 34 (2021) 8780–8794.
[56] T. Chen, R. Zhang, G. Hinton, Analog bits: Generating discrete data using diffusion models with self-conditioning, in: The 11th International Conference on Learning Representations, openreview.net, 2022.
[57] J. Ho, A. Jain, P. Abbeel, Denoising diffusion probabilistic models, Adv. Neural Inf. Process. Syst. Curran Assoc. 33 (2020) 6840–6851.
[58] J. Ho, T. Salimans., Classifier-free diffusion guidance, in: NeurIPS 2021 Workshop on Deep Generative Models and Downstream Applications, openreview. net, 2021.
[59] X.Y. Zheng, H. Pan, P.S. Wang, X. Tong, Y. Liu, H.Y. Shum, Locally attentional SDF diffusion for controllable 3D shape generation, ACM Trans. Graph. (ToG) 42 (4) (2023) 1–13, ACM NewYork, NY, USA.
[60] L. Wang, J. Boddapati, K. Liu, P. Zhu, C. Daraio, W. Chen, Mechanical cloak via data-driven aperiodic metamaterial design, Proc. Natl. Acad. Sci. USA 119 (13) (2022) e2122185119.
[61] N. Komodakis, N. Paragios, G. Tziritas, MRF energy minimization and beyond via dual decomposition, IEEE Trans. Pattern Anal. Mach. Intell. 33 (3) (2010) 531–552, IEEE.
[62] Z. Hashin, S. Shtrikman, On some variational principles in anisotropic and nonhomogeneous elasticity, J. Mech. Phys. Solids 10 (4) (1962) 335–342.
[63] A. Bansal, H.M. Chu, A. Schwarzschild, S. Sengupta, M. Goldblum, J. Geiping, T. Goldstein, Universal guidance for diffusion models, in: Proceedings of the IEEE/CVF Conference on Computer Vision and Pattern Recognition, 2023, pp. 843–852.